

PAPER

View Article Online
View Journal | View IssueCrossMark
click for updatesCite this: *J. Mater. Chem. A*, 2015, 3, 22094Unique synthesis of mesoporous peapod-like $\text{NiCo}_2\text{O}_4\text{-C}$ nanorods array as an enhanced anode for lithium ion batteries†

Liang Peng, Huijuan Zhang, Yuanjuan Bai, Jiao Yang and Yu Wang*

A novel peapod-like $\text{NiCo}_2\text{O}_4\text{-C}$ nanorods array on a 3D Ni-foam was synthesized for the first time and used as an anode for lithium ion batteries. The nanorods array was grown directly on a 3D Ni-foam by a facile route, including a hydrothermal reaction and subsequent annealing at a setting temperature. In contrast to previous reports, the as-prepared peapod-like $\text{NiCo}_2\text{O}_4\text{-C}$ composite in our experiments exhibited both mesoporosity and excellent conductivity; moreover, the stable core-shell structure allowed improved electron transfer and electrolyte penetration when applied to lithium ion batteries. When tested in an electrochemical system, the as-prepared samples demonstrated excellent electrochemical performance such as enhanced rate capability (a reversible capability of 664 mA h g^{-1} at 2000 mA g^{-1}) as well as a high coulombic efficiency (coulombic efficiency of 97% can be obtained after 200 cycles at 100 mA g^{-1}).

Received 31st August 2015
Accepted 17th September 2015

DOI: 10.1039/c5ta06877k

www.rsc.org/MaterialsA

Introduction

Due to the growing concerns of increased oil prices, environmental issues and the stretched energy situation, various energy storage systems have been designed and presented, especially electrochemical energy storage devices, which have been studied extensively and identified as promising green energy storage systems.^{1,2} Lithium ion batteries (LIBs), especially with a high rate, long lifespan and high energy density properties, are considered the most important energy storage and conversion device such as portable electric devices and electric vehicles.³

LIBs consist of four parts: cathode electrode, anode electrode, separator and electrolyte.^{4,5} Recently, various active materials have been studied for LIBs as anode or cathode materials, including metal (Sn),⁶ metal oxides (CuO , Fe_2O_3 , SnO_2 , and NiCo_2O_4),⁷⁻⁹ metal sulfides (CoS and MoS_2),^{10,11} carbon materials (graphene and carbon nanotube),^{12,13} conducting polymers (polypyrrole, polyaniline and polythiophene),^{14,15} silicon,¹⁶ and sulphur.^{17,18} Among these abovementioned active materials, transition metal oxides have important properties of semiconductors with extensive applications in energy storage due to their unique electrochemical performance. However, acting as an alternative promising anodic material for LIBs, the properties of NiCo_2O_4 have received less attention.^{19,20} As a LIBs anode material, NiCo_2O_4

can react with eight Li-ion per formula unit with a high theoretical capacity of $\sim 890 \text{ mA h g}^{-1}$. Moreover, as a binary metal oxide, NiCo_2O_4 has much better electrical conductivity and electrochemical performance than single cobalt oxides or nickel oxides.^{19,21} The higher electrical conductivity, which is favorable for rapid electrons transfer in an electrode, can achieve much higher specific capacity and better cycling performance. In addition to the abovementioned advantages, other features, such as abundant resources, low-cost, environmental friendliness, and can be obtained from both cobalt and nickel ions, also highlight its promising electrochemical capacitors (ECs) applications as an alternative anode electrode in Li-ion batteries.

However, large volume changes appear during Li-ion charge-discharge process due to the conversion reaction mechanism, which lead to the pulverization of electrode materials and detachment from the current collector, resulting in poor cycling performance.²²⁻²⁴ In attempt to solve this problem, it is an efficient way to design porous nanostructures with highly accessible surfaces and unique sizes and morphologies.^{25,26} With the merit of mesopores, electrodes materials can exhibit superior electrochemical performance because of their high specific surface areas, which increases the interface contact between the electrode and electrolyte and allows the electrolyte to permeate into the electrode materials easily, leading to a great flux of Li-ion across the interface and providing effective space for volume expansion during the charge-discharge cycle. The other effective strategy to solve the abovementioned problem is to prepare nanostructured materials with a thin coating of conducting material, including origin poly-layer, carbon layer, and metal layers.²⁷⁻²⁹ Owing to the protection by the coating-layers,

The State Key Laboratory of Mechanical Transmissions and School of Chemistry and Chemical Engineering, Chongqing University, Chongqing 400044, China. E-mail: wangy@cqu.edu.cn; prospectwy@gmail.com

† Electronic supplementary information (ESI) available: More EDS, Raman, XPS, TEM-mapping dates. See DOI: 10.1039/c5ta06877k

the NiCo_2O_4 anode material can relieve the stress induced by volume expansion or contraction, and then obtain improved capacity retention. In addition, the introduction of coating-layers can also increase the electronic conductivity and avoid the aggregation and pulverization of the NiCo_2O_4 anode material during the Li-ion insertion-extraction process.

In the present study, we introduce a facile approach to prepare a unique peapod-like architectural array with NiCo_2O_4 nanoparticles encapsulated in carbon nanorods and grown directly on the 3D Ni-foam. The unique peapod-like nanocomposite array has various admirable characteristics, including small size of the peapods, good graphitization of carbon fibers, remarkable mesoporous property and stable nanostructure. All these advantages sufficiently verify the excellent performance in the electrochemical measurements of LIBs such as high charge-discharge capacities, excellent rate capabilities, and exemplary cycling performance. It is believed that this novel nanocomposite has potential applications in both the energy and power storage of Li-ion batteries.

Experimental section

Synthesis of Ni-Co precursor nanorods array on the Ni-foam

All materials or chemicals were used as received and were of analytical grade. In a typical experiment,^{30,31} Ni-Co precursor nanorods array was synthesized on Ni-foam using a simple hydrothermal method. The experimental details are as follows: 10 mL $\text{Ni}(\text{NO}_3)_2 \cdot 6\text{H}_2\text{O}$ (0.2 mol L^{-1}), 10 mL $\text{Co}(\text{NO}_3)_2 \cdot 6\text{H}_2\text{O}$ (0.4 mol L^{-1}), 10 mmol NH_4F , and 15 mmol urea were dissolved in 20 mL deionized water (DI-water) and stirred to form a pink solution. The Ni-foam ($1.0 \text{ cm} \times 3.0 \text{ cm}$) was cleaned carefully with a concentrated HCl solution with ultrasonic treatment for 10 min, and then further cleaned by DI-water and absolute ethanol to ensure the surface of the Ni-foam was well cleaned. The abovementioned aqueous reagent solution and the Ni-foam substrate were then placed in a 50 mL Teflon-lined stainless-steel autoclave. The autoclave was sealed and maintained at 120°C for 9 h, and then cooled to room temperature. The array precursors were collected and rinsed several times with DI-water and absolute ethanol, and dried at 60°C in a vacuum drying oven for 12 h to obtain the precursors (Ni-Co precursors).

Synthesis of the peapod-like NCO-C nanorods array on Ni-foam

The Ni-Co precursors on a Ni-foam ($1.0 \text{ cm} \times 3.0 \text{ cm}$) was mixed ultrasonically with a 5 mL glucose aqueous solution (1 mol g^{-1}) and 35 mL DI-water for 10 min, and then transferred to a 50 mL Teflon-lined autoclave.^{32,33} The autoclave was sealed and maintained at 180°C for 6 h and then cooled to room temperature. Furthermore, the samples were collected and rinsed several times with DI-water and absolute ethanol. The Ni-Co precursors were coated with polymerized glucose molecules on the surface. The coating precursors were then annealed at 700°C for 200 min in a H_2 atmosphere and annealed at 250°C for 100 min at a ramping rate of 2°C min^{-1} to form the peapod-like structure composite, where the NiCo_2O_4

nanoparticles encapsulated the carbon nanorods on the 3D Ni-foam.³⁴

Carbon content tests

To precisely calculate the performances of LIBs, we also fabricated the peapod-like NCO-C nanorods array on a flat Ni-sheet and then scraped off the nanocomposite using a thin knife. Furthermore, the NCO-C samples (200 mg) were mixed uniformly with a concentrated HCl solution for 2 days to completely dissolve the NiCo_2O_4 nanoparticles. The remaining carbon was collected carefully, rinsed and dried in a vacuum drying oven at 60°C overnight. The carbon content in the NCO-C samples was calculated using the following formula:

$$C\% = [W_{(\text{C})}/W_{(\text{NCO-C})}] \times 100\%$$

where $W_{(\text{C})}$ and $W_{(\text{NCO-C})}$ are the weights of the remaining carbon and primary peapod-like samples, respectively. Using this method, the concentration of carbon in the nanocomposite was about 5.9 wt%, which makes a very low contribution to the capacity during the electrochemical tests.

Material characterizations

The fabricated materials were characterized by powder X-ray diffraction (Bruker D8 Advance X-ray diffractometer) with Cu $K\alpha$ radiation, scanning electron microscopy (SEM, JEOL, JSM-7800F) with energy dispersive spectrometry (EDS), transmission electron microscopy (TEM, JEOL, JEM-2100F), Brunauer-Emmett-Teller surface-area and pore-size analysis (BET, Quantachrome Autosorb-6B), Raman spectroscopy (RENISHAW Invia Raman Microscope, voltage (AC) 100–240 V, power 150 W) and X-ray photoelectron spectroscopy (XPS, ESCALAB 250Xi).

Electrochemical measurements

Electrochemical measurements were performed with R2032 coin-type cells. A Ni-foam loaded with NCO-C nanosheets array was cut into smaller pieces ($1 \text{ cm} \times 1 \text{ cm}$) and used as binder-free working electrodes directly. A lithium metal was used as the counter and reference electrode and a Celgard 2400 membrane was used as the cell separator. The electrolyte was 1 M LiPF_6 in ethylene carbonate and diethyl carbonate (EC-DEC, v/v = 1 : 1). The cells were constructed in an Ar-filled glove box. The galvanostatic cycling was performed on Neware battery testing system, and cyclic voltammetry (CV) was collected using an Autolab (model of AUT71740). The electrochemical impedance measurements were carried out by applying an AC voltage of 5 mV in the frequency from 0.01 Hz to 100 kHz. The specific capacity and current density were calculated based on the mass of the active material in the working electrode. The electrochemical tests were carried out using a three electrode system.

Results and discussion

Structural and morphological characterization

Fig. 1 displays schematically the fabrication route and the final unique electrode architectures developed in this study. First, as

the typical synthesis process, the Ni-Co polymerized nanorods precursor (Ni-Co precursors) was grown vertically on 3D Ni-foam by a hydrothermal reaction.^{31,35} A thin layer of carbonized glucose molecule on the Ni-Co precursor surface was grown *via* a hydrothermal treatment using glucose as a green carbon source. The carbonized glucose coating precursors were then annealed in a CVD and Muffle-furnace oven at the corresponding elevated temperatures in Ar and air atmospheres, respectively, resulting in the final peapod-like samples (NCO-C).

Scanning electron microscopy (SEM) was employed to investigate the morphologies and structures of the Ni-Co precursors. As shown in Fig. 2a, the nanorods precursor was grown fully and uniformly on the Ni-foam with a high density. In the locally magnified SEM image, as shown in Fig. 2b, some nanorods with a uniform diameter of about $\sim 10\text{--}30\text{ nm}$ could be found. These nanorods grew directly on the Ni-foam and along the same direction with a certain distance interval, which is favorable for the subsequent glucose molecule coating. The film cross-sectional image in Fig. 2c indicates that the nanorods precursor grew vertically on the Ni-foam substrate and the length of these nanorods was about $\sim 2.5\text{ }\mu\text{m}$. Fig. 2d clearly reveals good and tightening contact between the Ni-Co precursors and Ni-foam. A wide X-ray diffraction angle of $2\theta = 20\text{--}70^\circ$ (XRD), as shown in Fig. S1,[†] proved the coexistence of $\text{Co}_2(\text{CO}_3)(\text{OH})_2 \cdot 0.11\text{H}_2\text{O}$ (JCPDS: 48-0083) and $\text{Ni}_2(\text{CO}_3)(\text{OH})_2 \cdot 4\text{H}_2\text{O}$ (JCPDS: 38-0714) in the Ni-Co precursors.

More information on the surface electronic states of the as-prepared NCO-C can be further characterized by X-ray photoelectron spectroscopy (XPS) and the corresponding results are presented in Fig. S2.[†] The high-resolution spectrum for the O 1s region (Fig. S2a[†]) indicated two oxygen contributions. In general, the peak at 531.2 eV is associated with defects, contaminants and a number of surface species, such as hydroxyls, chemisorbed oxygen, under-coordinated lattice oxygen, or intrinsic species to the surface of the spinel. In particular, the peak at 529.4 eV is typical of metal-oxygen bonds.³⁶ Using the Gaussian fitting method, the Ni 2p emission spectrum (Fig. S2b[†]) was best fitted by two spin-orbit doublets, which are characteristic of Ni^{2+} and Ni^{3+} , and two shakeup satellite peaks (denoted as "sat.").^{37,38} In addition, the Co 2p

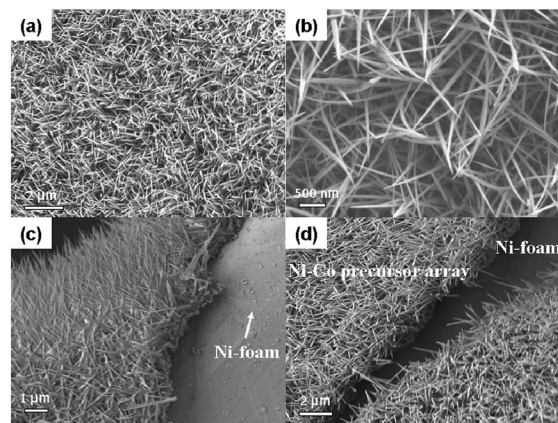


Fig. 2 (a) Low-magnification SEM image of the top view of the Ni-Co precursor. (b) and (c) Cross-section views to reveal the uniform 1-D nanorod structure of the Ni-Co precursor. (d) Enlarged SEM image to disclose the regular aligned structure.

spectrum was also best fitted considering two spin-orbit doublets, which are characteristic of Co^{2+} and Co^{3+} , and two couples of shakeup satellites (Fig. S2c[†]).³⁹ The composition and phase purity of the NCO-C composite were characterized by XRD and the result showed that all the reflection peaks could be indexed to cubic NiCo_2O_4 with a special spinel structure corresponding to the JCPDF card (no. 20-0781) (Fig. 3), and no additional peaks could be detected implying that the final samples had been fabricated without impurities.^{40,41} In addition, the NCO-C composite was scraped off the Ni-foam and further examined by energy-dispersive X-ray spectroscopy (EDX) (Fig. S3[†]), which reveals an atomic Ni/Co ratio of 1 : 2, wherein Si is from the silicon wafer.

SEM and TEM were employed to investigate the as-collected samples, as shown in Fig. 4. Fig. 4a showed that the NCO-C samples could be prepared on a large scale using our synthetic method, and 1-D nanostructures with a uniform morphology could be produced. As shown in Fig. 4b, these 1-D nanostructures originated from the same starting point and grew along the common direction, which is almost perpendicular to

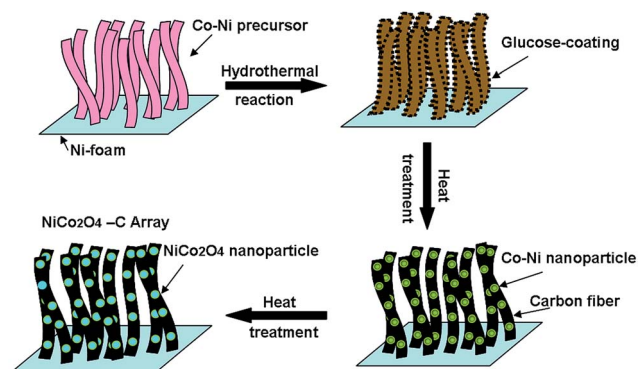


Fig. 1 Schematic of the synthesis of the peapod-like $\text{NiCo}_2\text{O}_4\text{--C}$ nanorods array on 3D Ni-foam.

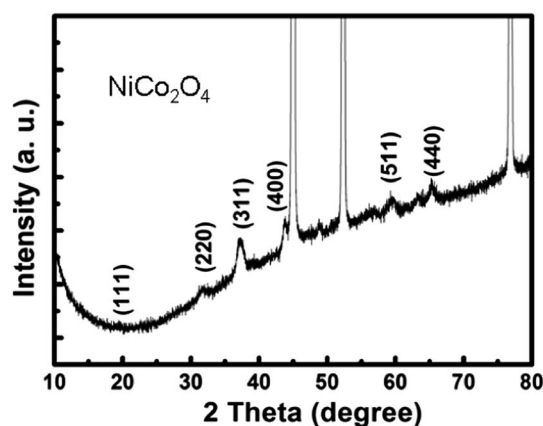


Fig. 3 XRD patterns of the obtained pure-phase NiCo_2O_4 on the Ni-foam (JCPDS 20-0781).

the surface of the Ni-foam. The corresponding magnified image shown in Fig. 4c shows that the samples exhibit a uniform nanorod-shaped morphology with a certain distance interval to each other. The high-magnification SEM image (Fig. 4d) indicates that many peapod-like nanorods are aligned together, and the encapsulated NiCo_2O_4 nanoparticles can be observed clearly with their distribution along the carbon rod. Another cross-section SEM image (shown in Fig. 4e) showed that the length of the as-prepared NCO-C nanorods composite is around 2 μm . To further reveal the structural details of the NCO-C composite, TEM was performed, as shown in Fig. 4f-h. From Fig. 4f and g, especially in Fig. 4g, it can be observed that all the samples possessed a peapod-like configuration, wherein isolated NiCo_2O_4 nanoparticles were separated from each other and distributed uniformly in the corresponding carbon rod with regular interval distance of 10–30 nm. The HRTEM image (Fig. 4h) of the ultimate products of the NCO-C composite shows that the encapsulated well-crystallized NiCo_2O_4 nanoparticles are coated with carbon layers to form 1-D hierarchical structures. The distances of 0.47 and 0.28 nm correspond to their equivalent crystal planes of (111) and (220) for spinal

NiCo_2O_4 , respectively.^{42,43} The image shows that the ultimately synthesized NCO-C composite maintain the morphology of the peapod-like nanorods array during the annealing in air.^{32,33} Furthermore, the corresponding TEM-EDS elemental mapping analysis of the NCO-C composite also confirmed the NCO-C hierarchical nanostructure, as shown in Fig. S4,† wherein the mappings for Ni, Co, O and C show a good distribution of elements in the composite.

The specific surface area and porous distribution of the NCO-C composite are determined by nitrogen-adsorption/desorption analysis at 77 K, which is shown in Fig. 5. As shown in Fig. 5a, a typical Langmuir type IV isotherm with an apparent hysteresis loop can be observed, which demonstrates the mesoporous nature of the as-prepared sample.⁴⁴ Fig. 5a shows that the composite exhibits a high Brunauer–Emmett–Teller (BET) specific surface area of $200.75 \text{ m}^2 \text{ g}^{-1}$. The porous size distribution calculated from the adsorption isotherm using the BJH model (Fig. 5b) indicates that most pore sizes fall into the range of 2–5 nm, and the pores size centered at 3 nm.⁴⁵ In fact, the mesoporosity could be reasonably inferred from the release of CO , CO_2 , H_2O and ammonia during thermal decomposition of

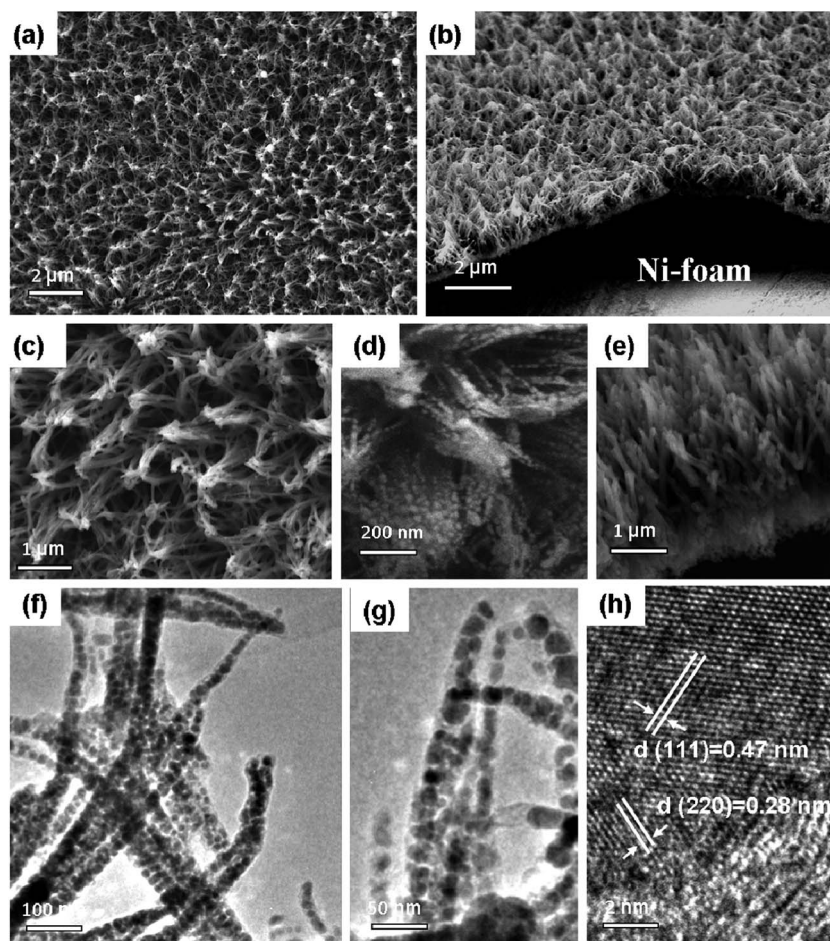


Fig. 4 (a) Typical SEM image showing the large scale production of the peapod-like NCO-C composite. (b) and (d) Cross-section views of the peapod-like NCO-C composite. (c) Low-magnification SEM image showing the unique peapod-like structure. (e) Enlarged SEM image of the specific structure. (f) and (g) Typical TEM images of the peapod-like structure, in which the NiCo_2O_4 nanoparticles are embedded uniformly in the carbon shell. (h) HRTEM image to characterize the crystal structures of the embedded NiCo_2O_4 nanoparticles and graphitized carbon shell.

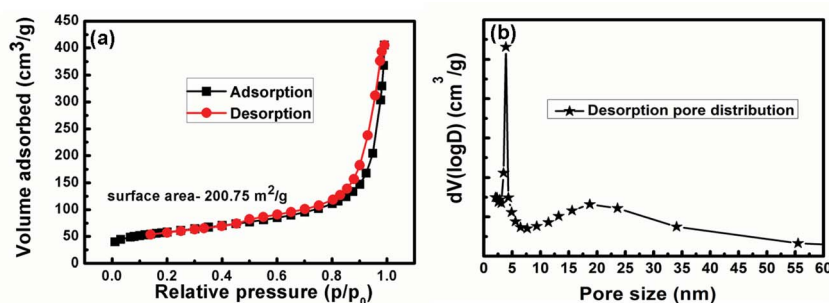


Fig. 5 (a) BET diagram proving high surface area for the peapod-like NCO-C composite and (b) corresponding pore size distribution.

the Ni-Co precursor. Such a porous nanostructure could effectively improve the electrochemical performances of the electrode materials because it can greatly enhance the diffusion of electrolyte to the electrode materials and buffer the large volume change in the anode during the fast charge-discharge cycles. Raman spectroscopy is used to characterize the state of carbon in the peapod-like composite (shown in Fig. S5†). Two main bands are observed at around 1590 and 1380 cm^{-1} , which were assigned to the G band and D band, respectively. The G band corresponds to the graphite in-plane vibrations with E_{2g} symmetry, whereas the D band was attributed to disorder-allowed phonon modes. Usually, the ratio value I_D/I_G can be used to evaluate the degree of disorder for a carbon layer structure. As the I_D/I_G ratio increases, the defect structure increases, meaning the degree of graphitization becomes low.^{46,47} The value of I_D/I_G for the NCO-C composite is around ~ 1 , which suggests that carbon has a relatively high degree of graphitization.

Electrochemical characteristics

The electrochemical performance measurements of the NCO-C composite are configured as CR2032 coin cells without using ancillary binders or conducting additives. Fig. 6a shows the cyclic voltammetry (CV) curves of the electrodes at a scanning rate of 0.5 mV s^{-1} in the voltage of 0.01–3.0 V (vs. Li/Li^+). Usually, the voltammogram for the first cycle is different from that of the others. In the first cathodic scan, the intense peak at 0.86 V can be considered as the reduction of Co^{3+} and Ni^{2+} to the corresponding metallic Co and Ni. In the subsequent cycles, the main reduction peaks shift to higher potential at 0.92 V. Moreover, the following anodic sweep is characterized by two oxidation peaks at ~ 1.6 V and 2.2 V, which can be attributed to the oxidation of Ni to Ni^{2+} and Co to Co^{3+} , respectively. On the basis of the cyclic voltammograms (CV) and together with the previous reports, the electrochemical cycles involved during the Li-ion insertion-extraction process can be classified as follows:^{22,48}

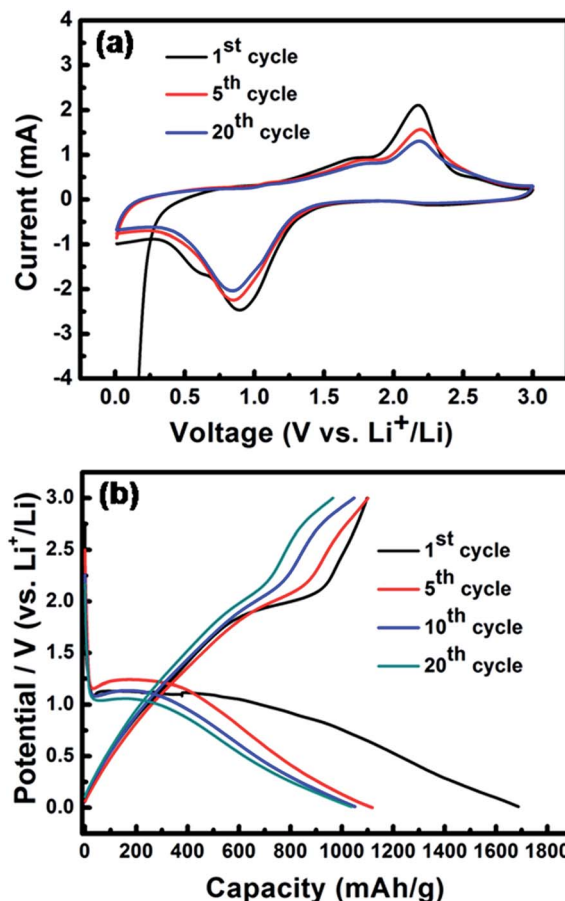
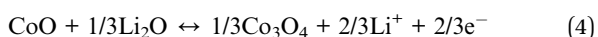
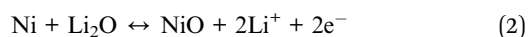


Fig. 6 (a) Cyclic voltammetry (CV) profiles of the peapod-like NCO-C composite, proving the thermodynamic stability. (b) Galvanostatic measurement curve at a current density of 100 mA g^{-1} .

The charge-discharge tests of the NCO-C anode electrode in the voltage window of 0.01–3.0 V (vs. Li/Li^+) at 100 mA g^{-1} are shown in Fig. 6b. The first discharge capacity is 1682 mA h g^{-1} , which is much higher than the theoretical capacity (890 mA h g^{-1}) greatly due to the formation of solid electrolyte interface (SEI) film and as well as forming a organic polymeric/gel-like layer by electrolyte decomposition.⁴⁹ In subsequent charge-discharge processes, the cycle profiles tend to be stable and indicate similar electrochemical performances with

approximate charge and discharge capacities of 1081 and 1152 mA h g⁻¹, respectively. Interestingly, these capacities are unexpectedly higher than the theoretical capacity, which is possible due to two reasons: (1) the reversible formation-dissolution of the polymer/gel-like film; (2) porous of the outside carbon fiber and inside active materials can provide some effective sites for Li⁺ insertion-extraction.

To better understand the electrochemical behavior of the NCO-C composite, we also studied its rate capability, as shown in Fig. 7a. The as-prepared NCO-C anode electrode was evaluated at various current densities (100 to 2000 mA g⁻¹). The discharge capacity can reach 1150 mA h g⁻¹ at a low rate current of 100 mA g⁻¹ after 10 cycles. When the current densities increased stepwise to 300, 500, 1000, and 2000 mA g⁻¹, the

results showed good rate capability with an average discharge capacity of 984, 918, 764, and 653 mA h g⁻¹, respectively. Upon altering the current density back to 300 and 100 mA g⁻¹, the discharge capacities of 963 and 1024 mA h g⁻¹ can be obtained. Fig. 7b presents the capacity retention and coulombic efficiency of the NCO-C composite. After 200 cycles, the NCO-C composite electrode still exhibited a stable discharge capacity of 1183 mA h g⁻¹ (about 97% of the second discharge capacity), which is mostly because the unique core-shell structure can effectively alleviate the pulverization problem.

The cyclic performance of the NCO-C composite at currents of 500 and 2000 mA g⁻¹ are further demonstrated in Fig. 7c. The first capacities of the NCO-C composite were 1081 and 884 mA h g⁻¹ at the current densities of 500 and 2000 mA g⁻¹, respectively, and showed that there is a trend of gradually stable capacities after 10 and 50 cycles at a rate of 500 and 2000 mA g⁻¹, respectively. After 200 cycles, the discharge capacities were retained at 863 and 594 mA h g⁻¹ at current densities of 500 and 2000 mA g⁻¹, respectively, which are almost 96% and 67% of the theoretical capacities. As shown in Fig. S6,[†] the randomly dispersed peapod-like NCO-C composites, which are scraped off from the Ni-foam, were tested at a current density of 500 mA h g⁻¹. With the development of galvanostatic measurement, the specific capacity was finally retained 849 mA h g⁻¹ after 200 cycles, which is lower than that of the peapod-like composite grown directly on Ni-foam (863 mA h g⁻¹). We also compared the current study with other NiCo₂O₄-based high rate electrode materials reported in recent studies, such as hierarchical NiCo₂O₄ nanowire arrays,⁵⁰ porous NiCo₂O₄ nanoplates,⁵¹ mesoporous NiCo₂O₄ nanosheets,^{40,52} flower-like NiCo₂O₄,²² NiCo₂O₄ nanoparticles embedded in 3DHPC,⁴¹ NiCo₂O₄ mesoporous microsphere,⁵³ hollow NiCo₂O₄ nanocube,⁵⁴ and quasi-single-crystalline NiCo₂O₄ nanoribbons^{55,56} and these results are shown in Fig. 8. By comparison, these peapod-like NCO-C nanorods array composites showed comparable electrochemical performance at various rate densities to commonly electrodes.

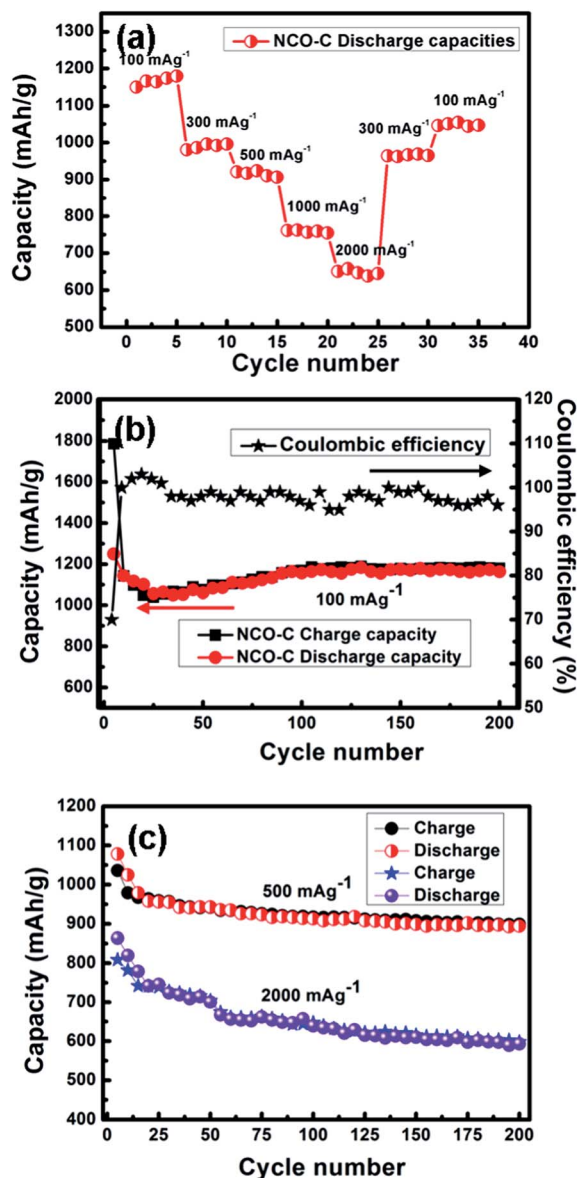


Fig. 7 (a) Rate capability test on the peapod-like NCO-C nanorods array on the Ni-foam and (b) corresponding coulombic efficiency. (c) Cycling performances of the peapod-like array at the current densities of 500 and 2000 mA g⁻¹.

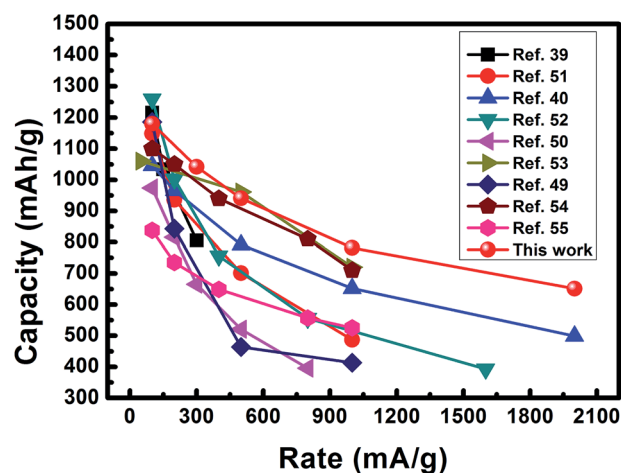


Fig. 8 Comparison of the rate capability of peapod-like NCO-C nanorods array with other NiCo₂O₄-based anode materials reported recently.

Conclusion

In summary, we successfully developed a novel route toward NCO–C nanorods array grown directly on a 3D Ni-form substrate and produced a binder free electrode for LIBs. The unique hierarchical nanostructure of the NCO–C composite combines the fascinating characters, including nano-size NiCo_2O_4 particles, large specific surface area, good conductivity, and good structure stability of the nanorod arrays. Owing to the abovementioned advantages, the NCO–C composite exhibits excellent electrochemical performance such as excellent rate capability (a reversible capability of 664 mA h g^{-1} at 2000 mA g^{-1}) as well as a high coulombic efficiency (about coulombic efficiency of 97% can be obtained after 200 cycles at 100 mA g^{-1}).

Acknowledgements

This study was financially supported by the Thousand Young Talents Program of the Chinese Central Government (Grant No. 0220002102003), the National Natural Science Foundation of China (NSFC, Grant No. 21373280, 21403019), the Fundamental Research Funds for the Central Universities (0301005202017), the Beijing National Laboratory for Molecular Sciences (BNLMS) and the Hundred Talents Program at Chongqing University (Grant No. 0903005203205).

References

- 1 N. Oyama, T. Tatsuma, T. Sato and T. Sotomura, *Nature*, 1995, **373**, 598–600.
- 2 W. Li, J. R. Dahn and D. S. Wainwright, *Science*, 1994, **264**, 1115–1118.
- 3 K. S. Kang, Y. S. Meng, J. Breger, C. P. Grey and G. Ceder, *Science*, 2006, **311**, 977–980.
- 4 M. J. Zou, M. Yashio, S. Gopukumar and J. I. Yamaki, *Chem. Mater.*, 2005, **17**, 1284–1286.
- 5 P. Balaya, *Energy Environ. Sci.*, 2008, **1**, 645–654.
- 6 N. Zhang, Q. Zhao, X. P. Han, J. G. Yang and J. Chen, *Nanoscale*, 2014, **6**, 2827–2832.
- 7 P. C. Lian, S. Z. Liang, X. F. Zhu, W. S. Yang and H. H. Wang, *Electrochim. Acta*, 2011, **58**, 81–88.
- 8 Y. M. Sun, X. L. Hu, W. Luo and Y. H. Huang, *J. Phys. Chem. C*, 2012, **116**, 20794–20799.
- 9 J. S. Xu and Y. J. Zhu, *ACS Appl. Mater. Interfaces*, 2012, **4**, 4752–4757.
- 10 X. P. Fang, C. X. Hua, X. W. Guo, Y. S. Hu, Z. X. Wang, X. P. Gao, F. Wu, J. Z. Wang and L. Q. Chen, *Electrochim. Acta*, 2012, **81**, 155–160.
- 11 W. W. Chen, T. T. Li, Q. Hu, C. P. Li and H. Guo, *J. Power Sources*, 2015, **286**, 159–165.
- 12 Z. L. Wang, D. Xu, H. G. Wang, Z. Wu and X. B. Zhang, *ACS Nano*, 2013, **7**, 2422–2430.
- 13 F. Liu, S. Y. Song, D. F. Xue and H. J. Zhang, *Adv. Mater.*, 2012, **24**, 1089–1094.
- 14 F. Wu, J. Z. Chen, L. Li, T. Zhao, Z. Liu and R. J. Chen, *ChemSusChem*, 2013, **6**, 1438–1444.
- 15 L. Yang, V. A. Mihali, D. Brandell, M. Stromme and M. Sjodin, *J. Phys. Chem. C*, 2014, **118**, 25956–25963.
- 16 H. Yoo, J. I. Lee, H. Kim, J. P. Lee, J. Cho and S. Park, *Nano Lett.*, 2011, **11**, 4324–4328.
- 17 S. Xin, L. Gu, N. H. Zhao, Y. X. Yin, L. J. Zhou, Y. G. Guo and L. J. Wan, *J. Am. Chem. Soc.*, 2012, **134**, 18510–18513.
- 18 Y. S. Su, Y. Z. Fu and A. Manthiram, *Phys. Chem. Chem. Phys.*, 2012, **14**, 14495–14499.
- 19 X. Xu, B. Dong, S. Ding, C. Xiao and D. Yu, *J. Mater. Chem. A*, 2014, **2**, 13069–13074.
- 20 L. Shen, L. Yu, X. Y. Yu, X. Zhang and X. W. Lou, *Angew. Chem., Int. Ed.*, 2015, **54**, 1868–1872.
- 21 A. K. Mondal, D. Su, S. Chen, X. Xie and G. Wang, *ACS Appl. Mater. Interfaces*, 2014, **6**, 14827–14835.
- 22 L. Li, Y. Cheah, Y. Ko, P. Teh, G. Wee, C. Wong, S. Peng and M. Srinivasan, *J. Mater. Chem. A*, 2013, **1**, 10935–10945.
- 23 Y. G. Li, B. Tan and Y. Y. Wu, *Nano Lett.*, 2008, **8**, 265–270.
- 24 X. Y. Chen, H. L. Zhu, Y. C. Chen, Y. Y. Shang, A. Y. Cao, L. B. Hu and G. W. Rubloff, *ACS Nano*, 2012, **6**, 7948–7955.
- 25 S. Xiong, J. S. Chen, X. W. Lou and H. C. Zeng, *Adv. Funct. Mater.*, 2012, **22**, 861–871.
- 26 Y. Wang, H. Xia, L. Lu and J. Y. Lin, *ACS Nano*, 2010, **4**, 1425–1432.
- 27 W. H. Shi, J. X. Zhu, X. H. Rui, X. H. Cao, C. Chen, H. Zhang, H. H. Hng and Q. Y. Yan, *ACS Appl. Mater. Interfaces*, 2012, **4**, 2999–3006.
- 28 A. Trifonova, M. Winter and J. O. Besenhard, *J. Power Sources*, 2007, **174**, 800–804.
- 29 S. T. Myung, K. Izumi, S. Komaba, H. Yashiro, H. J. Bang, Y. K. Sun and N. Kumagai, *J. Phys. Chem. C*, 2007, **111**, 4061–4067.
- 30 G. Q. Zhang, H. B. Wu, H. E. Hoster, M. B. Chan-Park and X. W. Lou, *Energy Environ. Sci.*, 2012, **5**, 9453–9456.
- 31 D. Cai, B. Liu, D. Wang, L. Wang, Y. Liu, H. Li, Y. Wang, Q. Li and T. Wang, *J. Mater. Chem. A*, 2014, **2**, 4954–4960.
- 32 L. Peng, Y. Feng, Y. Bai, H.-J. Qiu and Y. Wang, *J. Mater. Chem. A*, 2015, **3**, 8825–8831.
- 33 Y. Wang, H. J. Zhang, L. Lu, L. P. Stubbs, C. C. Wong and J. Y. Lin, *ACS Nano*, 2010, **4**, 4753–4761.
- 34 H. J. Zhang, Y. J. Bai, Y. Zhang, X. Li, Y. Y. Feng, Q. Liu, K. Wu and Y. Wang, *Sci. Rep.*, 2013, **3**, 2717.
- 35 K. Xu, W. Li, Q. Liu, B. Li, X. Liu, L. An, Z. Chen, R. Zou and J. Hu, *J. Mater. Chem. A*, 2014, **2**, 4795–4802.
- 36 X.-F. Lu, D.-J. Wu, R.-Z. Li, Q. Li, S.-H. Ye, Y.-X. Tong and G.-R. Li, *J. Mater. Chem. A*, 2014, **2**, 4706–4713.
- 37 C. An, Y. Wang, Y. Huang, Y. Xu, C. Xu, L. Jiao and H. Yuan, *CrystEngComm*, 2014, **16**, 385–392.
- 38 H. Shi and G. Zhao, *J. Phys. Chem. C*, 2014, **118**, 25939–25946.
- 39 T. F. Hung, S. G. Mohamed, C. C. Shen, Y. Q. Tsai, W. S. Chang and R. S. Liu, *Nanoscale*, 2013, **5**, 12115–12119.
- 40 A. K. Mondal, D. W. Su, S. Q. Chen, K. Kretschmer, X. Q. Xie, H. J. Ahn and G. X. Wang, *ChemPhysChem*, 2015, **16**, 169–175.
- 41 L. Wang, L. Zhuo, C. Zhang and F. Zhao, *ACS Appl. Mater. Interfaces*, 2014, **6**, 10813–10820.
- 42 G. Y. Huang, S. M. Xu, Z. H. Xu, H. Y. Sun and L. Y. Li, *ACS Appl. Mater. Interfaces*, 2014, **6**, 21325–21334.

- 43 T. Li, X. Li, Z. Wang, H. Guo and Y. Li, *J. Mater. Chem. A*, 2015, **3**, 11970–11975.
- 44 L. Shen, C. Yuan, H. Luo, X. Zhang, K. Xu and Y. Xia, *J. Mater. Chem.*, 2010, **20**, 6998–7004.
- 45 G.-N. Zhu, H.-J. Liu, J.-H. Zhuang, C.-X. Wang, Y.-G. Wang and Y.-Y. Xia, *Energy Environ. Sci.*, 2011, **4**, 4016–4022.
- 46 B. Li, C. Han, Y.-B. He, C. Yang, H. Du, Q.-H. Yang and F. Kang, *Energy Environ. Sci.*, 2012, **5**, 9595–9602.
- 47 L.-W. Zhang, H.-B. Fu and Y.-F. Zhu, *Adv. Funct. Mater.*, 2008, **18**, 2180–2189.
- 48 F. Zheng, D. Zhu and Q. Chen, *ACS Appl. Mater. Interfaces*, 2014, **6**, 9256–9264.
- 49 J. Y. Liao, X. Xiao, D. Higgins, G. Lui and Z. Chen, *ACS Appl. Mater. Interfaces*, 2014, **6**, 568–574.
- 50 G. Chen, J. Yang, J. Tang and X. Zhou, *RSC Adv.*, 2015, **5**, 23067–23072.
- 51 Y. Chen, M. Zhuo, J. Deng, Z. Xu, Q. Li and T. Wang, *J. Mater. Chem. A*, 2014, **2**, 4449–4456.
- 52 Y. Chen, J. Zhu, B. Qu, B. Lu and Z. Xu, *Nano Energy*, 2014, **3**, 88–94.
- 53 J. Li, S. Xiong, Y. Liu, Z. Ju and Y. Qian, *ACS Appl. Mater. Interfaces*, 2013, **5**, 981–988.
- 54 H. Guo, L. Liu, T. Li, W. Chen, J. Liu and Y. Guo, *Nanoscale*, 2014, **6**, 5491–5497.
- 55 B. S. Li, J. K. Feng, Y. T. Qian and S. L. Xiong, *J. Mater. Chem. A*, 2015, **3**, 10336–10344.
- 56 T. Li, X. Li, Z. Wang, H. Guo and Y. Li, *J. Mater. Chem. A*, 2015, **3**, 11970–11975.